

High-pressure stabilization of Mg_2IrH_7 : Structural proximity to high- T_c superconductivity

Shubham Sinha,^{1,*} Wencheng Lu,^{1,†} Mads F. Hansen,^{1,2} Michael J. Hutcheon,³ Trevor W. Bontke,⁴ Lewis J. Conway,^{5,6} Kapildeb Dolui,⁵ Chris J. Pickard,^{5,6} Christoph Heil,⁷ Piotr A. Guńka,⁸ Stella Chariton,⁹ Vitali Prakapenka,⁹ Liangzi Deng,⁴ Ching-Wu Chu,⁴ Matthew N. Julian,¹⁰ Rohit P. Prasankumar,¹⁰ and Timothy A. Strobel^{1,‡}

¹*Earth and Planets Laboratory, Carnegie Institution for Science,
5241 Broad Branch Road NW, Washington, DC 20015, USA*

²*Cavendish Laboratory, University of Cambridge,
JJ Thomson Avenue, Cambridge, CB3 0HE, United Kingdom*

³*Theory of Condensed Matter Group, Cavendish Laboratory,
J. J. Thomson Avenue, Cambridge CB3 0HE, United Kingdom*

⁴*Department of Physics and Texas Center for Superconductivity at the University of Houston, Houston, TX 77204, USA*

⁵*Department of Materials Science and Metallurgy, University of Cambridge,
27 Charles Babbage Road, Cambridge, CB3 0FS, UK*

⁶*Advanced Institute for Materials Research, Tohoku University, Sendai, 980-8577, Japan*

⁷*Institute of Theoretical and Computational Physics,
Graz University of Technology, NAWI Graz, 8010 Graz, Austria*

⁸*Faculty of Chemistry, Warsaw University of Technology, Noakowskiego 3, 00-664 Warszawa, Poland*

⁹*Center for Advanced Radiation Sources, The University of Chicago, Lemont, Illinois 60439, United States*

¹⁰*Enterprise Science Fund, Intellectual Ventures,
3150 139th Ave SE, Bellevue, WA, 98005, USA*

(Dated: March 2, 2026)

Mg_2IrH_6 is a metastable complex metal hydride with a predicted superconducting transition temperature as high as 170 K at ambient pressure. Following the synthesis of isomorphic, insulating Mg_2IrH_5 at low pressure, higher-pressure studies were conducted to investigate the phase behavior and compound formation in this system. X-ray diffraction and Raman spectroscopic measurements indicate that cubic Mg_2IrH_7 is stabilized above ca. 40 GPa and coexists with a related hexagonal hydride with likely composition near Mg_2IrH_5 . Electrical transport measurements show that cubic Mg_2IrH_7 is insulating, in agreement with *ab initio* predictions, and persists during room-temperature decompression until ~ 20 GPa before reverting back to cubic Mg_2IrH_5 . The experimental results confirm ground-state structure predictions in the Mg–Ir–H system, and the formation of two nearly identical phases with surrounding compositions opens new opportunities to access superconducting Mg_2IrH_6 through non-equilibrium processing pathways.

I. INTRODUCTION

Hydrides have helped achieve the long-sought goal of obtaining superconductivity near room temperature [1–7]. Nevertheless, these materials exhibit such behavior at extremely high pressures, often exceeding hundreds of gigapascals. The achievement of superconductivity at such high temperatures represents an important milestone in physics research, however the extreme pressures necessary place major limitations on potential future applications. Thus, novel strategies to stabilize these materials or create lower-pressure alternatives is an active research goal. Lower-pressure stabilization has been realized in some superconducting hydrides such as LaBeH_8 and LaB_2H_8 , as well as other classes of superconducting materials [8–11].

Recent calculations have proposed conventional high-

T_c superconductivity at ambient pressure in several complex metal hydride phases of the form A_xMH_y (where A is an alkali, alkaline-earth, or selected trivalent metal, and M is a transition metal, [12–15]), as well as perovskite hydrides such as AMH_3 [16, 17]. Some of these proposed materials are predicted to exhibit T_c well above 100 K. Indeed, prior experimental studies on complex hydrides such as compressed BaReH_9 and $\text{Li}_5\text{MoH}_{11}$ [18, 19], as well as low-pressure $\text{Mg}_4\text{Pt}_3\text{H}_6$ [20] show the possibility of metallic phases that can support superconductivity.

Among the proposed superconducting complex hydrides, Mg_2IrH_6 (Fig. 1) is a promising candidate with predictions of T_c up to 170 K [13]. This phase is predicted to be dynamically stable at ambient pressure and thermodynamically metastable by ~ 60 meV/atom. Metallic Mg_2IrH_6 is comprised of octahedral IrH_6 hydrido complexes (formally $[\text{IrH}_6]^{4-}$), surrounded by Mg^{2+} cations [13, 21]. High- T_c superconductivity arises from a significant contribution of H-1s states at a Van-Hove-like singularity near the Fermi level, allowing high-frequency phonons to couple with Fermi-surface electrons [12, 13, 22].

* ssinha@carnegiescience.edu

† wlu@carnegiescience.edu

‡ tstrobel@carnegiescience.edu

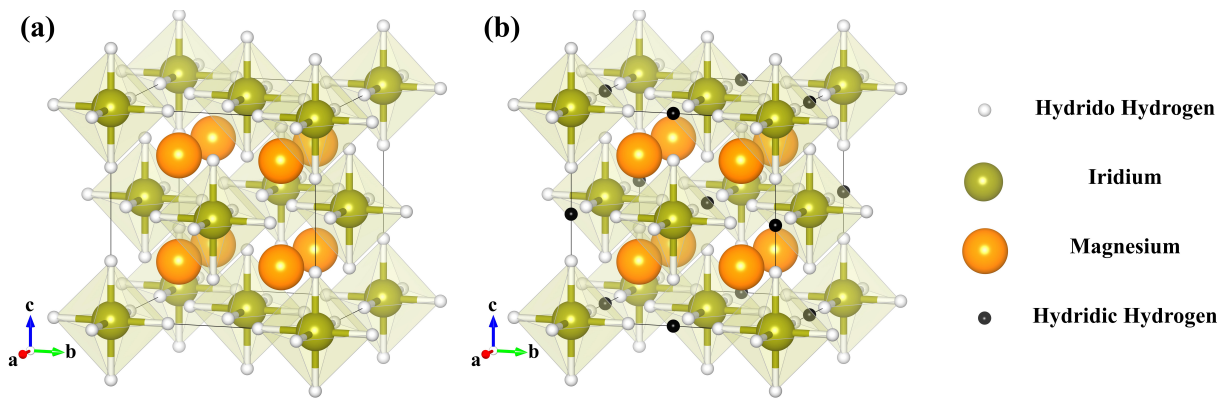


FIG. 1. The crystal structures of (a) FCC Mg_2IrH_6 and (b) FCC Mg_2IrH_7 . The structures are distinguished by an additional interstitial H per formula unit, shown in black.

Recent experimental investigations in the Mg–Ir–H system produced the compound Mg_2IrH_5 at pressures between 150 bar and ~ 30 GPa [21]. The FCC structure of Mg_2IrH_5 is isomorphic with Mg_2IrH_6 , but with an octahedral hydrogen site occupancy of $\frac{5}{6}$, resulting in disordered $[\text{IrH}_5]^{4-}$ complexes with a characteristic Ir–H Raman stretching mode near 2100 cm^{-1} at ambient pressure. The two Mg^{2+} cations per formula unit compensate the charge of the $[\text{IrH}_5]^{4-}$ complex anions, yielding a charge-balanced insulator. Mg_2IrH_5 is one hydrogen vacancy away from superconducting Mg_2IrH_6 , which might be achieved via low-barrier hydrogen insertion [21].

From another side, Mg_2IrH_6 might be obtained by hydrogen removal from FCC Mg_2IrH_7 . Mg_2IrH_7 was predicted to be thermodynamically stable above ~ 15 GPa, and the removal of a single interstitial hydridic hydrogen—the distinguishing structural feature between Mg_2IrH_6 —could enable the formation of the superconducting phase [13]. While Mg_2IrH_7 was predicted to be thermodynamically stable near 15 GPa, it was not observed experimentally to pressures around 30 GPa [21]. Configurational entropy of Mg_2IrH_5 , originating from the disordered $[\text{IrH}_5]^{4-}$ complexes, contributes to the stability of this phase and may alter the predicted ground-state phases at finite temperature [13]. Given that static calculations show the stability of Mg_2IrH_5 decreases above 15 GPa while Mg_2IrH_7 remains on the calculated convex hull, it is plausible that Mg_2IrH_7 becomes stabilized on basis of free energy at pressures high enough to overcome the configurational entropy contribution of Mg_2IrH_5 [13, 21].

In this study, we have conducted experiments on Mg_2IrH_5 to higher pressures near 40 GPa, finding that it transforms into FCC Mg_2IrH_7 in the presence of excess hydrogen. Mg_2IrH_7 is clearly distinguished from Mg_2IrH_5 by a strong $[\text{IrH}_6]^{3-}$ Raman stretching mode near $\sim 1500\text{ cm}^{-1}$, softened by roughly 800 cm^{-1} from the $[\text{IrH}_5]^{4-}$ units within Mg_2IrH_5 at 40 GPa, as well as an expanded FCC lattice volume. FCC Mg_2IrH_7 typically coexists with another energetically competitive

hexagonal hydride with composition likely near Mg_2IrH_5 . Mg_2IrH_7 persists during decompression until ~ 20 GPa, before reverting back to Mg_2IrH_5 . The observation of FCC Mg_2IrH_7 , which is nearly equivalent to Mg_2IrH_6 , presents additional opportunities to realize high- T_c hydride superconductivity at reduced-pressure conditions.

II. METHODS

Experimental synthesis. The Mg_2IrH_5 samples used as precursors in this study were synthesized by mixing Mg (Sigma Aldrich 99.5%) and Ir (Sigma Aldrich 99.9%) in a 2:1 molar ratio which were then heated inside a stainless steel autoclave-type reactor at $450\text{ }^\circ\text{C}$ under a hydrogen (UHP Airgas) pressure of ~ 150 bar for two weeks. The recovered precursor consisted of FCC Mg_2IrH_5 with small impurities of unreacted FCC Ir and a $Pm\bar{3}m$ MgIrH_x compound. Additional synthesis details can be found in reference [21].

High-pressure experiments were conducted using symmetric and BX90 diamond anvil cells (DACs) equipped with $300\text{ }\mu\text{m}$ culet anvils. Rhenium gaskets were indented to $40\text{ }\mu\text{m}$ and a $150\text{--}200\text{ }\mu\text{m}$ hole was laser drilled for the sample chamber. Thin pellets of the Mg_2IrH_5 precursor were created by pressing powder between two 1 mm culet anvils, small pieces from which were then loaded into the sample chamber and filled with either fluid H_2 at ~ 1.5 kbar, or ammonia borane, which served as a source for excess hydrogen. Sample pressures were estimated at room temperature using the diamond Raman edge or from a ruby chip placed in the sample chamber [23, 24].

Samples were compressed to target pressures near 40 GPa, and one- or two-sided laser heating was performed using a 1064 nm Nd:YAG laser [25]. It was found that low laser powers near the laser-coupling threshold ($\sim 800\text{ K}$) were sufficient to induce a structural transformation, and temperature estimations based on thermal emission were not viable in most low-power experiments. Additional heating at higher temperatures resulted in the

formation of a more complex hexagonal structure. Several heating tests were also performed using the $\sim 10\ \mu\text{m}$ of a CO_2 laser, which was found to produce equivalent results.

Raman spectroscopy. Unpolarized Raman spectra were measured using a 532 nm laser for excitation focused through a $20\times$ long-working-distance objective lens at a power of $\sim 5\ \text{mW}$, combined with a Princeton instruments SP2750 spectrograph with a 750 mm focal length.

X-ray diffraction. Angular-dispersive, monochromatic X-ray diffraction measurements were carried out in transmission geometry at 13-IDD (GSECARS) at the Advanced Photon Source using a wavelength of $0.3344\ \text{\AA}$ using a Pilatus3 X CdTe 1M detector. The sample-to-detector distance and detector geometry were calibrated using a LaB_6 standard, in conjunction with the Dioplas software [26], which was also used for data reduction. Preliminary diffraction measurements were also performed at beamline 12.2.2 [27] at the Advanced Light Source using a wavelength of $0.4959\ \text{\AA}$ using a Pilatus Si detector. For *in situ* diffraction measurements, pressure determination was established using the equation of state (EOS) of Ir [28] from small regions of unreacted sample near the laser heating spot, in addition to diamond Raman measurements [24]. To establish lattice parameters, Le Bail refinements of powder XRD data were performed using GSAS-II [29].

Crystalline diffraction spots were observed from a sample heated near 1500 K, which enabled multigrain analysis using a synchrotron beam size of $\sim 2\times 2\ \mu\text{m}$. Frames were recorded between an angular range of $\omega = -32^\circ$ to $+31^\circ$ in 0.5° steps with an exposure time of 1 s per frame. Reflections were harvested using CrysAlisPRO, assigned to individual grains with DAFi [30], and subsequently indexed and integrated using CrysAlisPRO software suite [31]. Crystal structures were solved with SHELXT 2018/2 and refinement was attempted using SHELXL 2018/3, invoked from within the Olex2 suite [32–34].

Electrical transport measurements. Non-magnetic DACs compatible with Quantum Design Physical Property Measurement System (PPMS model 6000) were utilized for electrical transport measurements with the maximum excitation current set to 1 mA. Two flat, $300\ \mu\text{m}$ culets were used with a Re gasket, which was indented to a thickness of $\sim 40\ \mu\text{m}$ and laser-drilled with a $\sim 280\ \mu\text{m}$ hole. A layer of cubic boron nitride (cBN)–epoxy composite was compressed for an insulation layer on one side of the gasket and then re-drilled with a $\sim 130\ \mu\text{m}$ hole for the sample chamber. The chamber was next filled with ammonia borane for the pressure medium and hydrogen source, in which a thin pellet of Mg_2IrH_5 was embedded. Pt electrodes cut from $12\ \mu\text{m}$ -thick foil were then placed onto the sample pellet in van der Pauw configuration for four probe measurement [35].

DFT calculations. Geometry optimizations and all subsequent calculations were performed using CASTEP [36] with the Perdew-Burke-Ernzerhof generalized gra-

dient approximation for solids (PBEsol) [37], a $600\ \text{eV}$ plane-wave cutoff, a k -point spacing of $2\pi\times 0.03\ \text{\AA}^{-1}$, and default CASTEP norm-conserving pseudopotentials (NCP). Structures were converged to give forces and stresses to within $0.05\ \text{eV}\cdot\text{\AA}^{-1}$ and $0.01\ \text{GPa}$. Gamma-point phonon and Raman intensity calculations were performed using density functional perturbation theory implemented in CASTEP [38] and QUANTUM ESPRESSO [39]. QUANTUM ESPRESSO calculations were performed using the Perdew-Burke-Ernzerhof (PBE) functional [40] and v1.5 of the GBRV pseudopotentials [41], with comparable parameters and tolerances to the CASTEP calculations.

III. RESULTS AND DISCUSSION

The Raman spectrum of Mg_2IrH_5 is characterized by an Ir–H stretching mode at $\sim 2100\ \text{cm}^{-1}$, Ir–H bending modes near $800\ \text{cm}^{-1}$, and lattice phonons at lower frequency [21]. When compressed to $38.7\ \text{GPa}$ at room temperature, these modes broaden significantly and the stretching vibration of $[\text{IrH}_5]^{4-}$ is detectable only as a shoulder near $\sim 2300\ \text{cm}^{-1}$ at the onset of the second-order diamond Raman peak (Fig. 2a). Gentle laser heating ($< 1000\ \text{K}$) of compressed Mg_2IrH_5 with a hydrogen source (either H_2 or ammonia borane) produced marked changes in the Raman spectrum. After heating at $38.7\ \text{GPa}$, a very intense peak appears at $1523\ \text{cm}^{-1}$, as well as three additional weaker, yet distinct peaks at 343 , 1174 and $2029\ \text{cm}^{-1}$ (Fig. 2a).

The strong Raman intensity of the peak at $1523\ \text{cm}^{-1}$ is suggestive of Ir–H stretching, and the frequency is consistent with the formation of $[\text{IrH}_6]^{3-}$ units based on comparison with other hydrido complexes MH_6 octahedral units (e.g., Mg_2FeH_6 , Ca_2RuH_6 , Sr_2RuH_6 , Eu_2RuH_6 , Mg_2OsH_6 , Na_3CoH_6 , and Rb_2PtH_6) [42–45]. The nearly $800\ \text{cm}^{-1}$ frequency shift from $[\text{IrH}_5]^{4-}$ is diagnostic of charge redistribution and strongly suggestive of a compound containing the $[\text{IrH}_6]^{3-}$ complex. Note that the DFT-relaxed Ir–H bond distance for $[\text{IrH}_6]^{3-}$ within $\text{Mg}_2\text{IrH}_7 / \text{Mg}_2\text{IrH}_6$ is $1.71\ \text{\AA}$, significantly elongated from $1.66\ \text{\AA}$ for $[\text{IrH}_5]^{4-}$ within Mg_2IrH_5 .

To help understand the structural transformation observed upon heating, we calculated the Raman frequencies and intensities for Mg_2IrH_7 , which was predicted to be the stable high-pressure phase at this Mg:Ir ratio [13]. The $Fm\bar{3}m$ structure possesses four Raman active phonons calculated at 310 (T_{2g}), 1139 (T_{2g}), 1687 (E_g) and 2142 (A_{1g}) cm^{-1} at $40\ \text{GPa}$. We note that Mg_2IrH_6 in the same space group possesses the same four Raman phonons at similar frequencies, but the second T_{2g} bending mode is softened by $\sim 200\ \text{cm}^{-1}$ in the absence of the interstitial hydrogen. The calculated frequencies of the four Raman modes for Mg_2IrH_7 are in good agreement with the four peaks observed experimentally, noting that the calculated frequencies under the static and harmonic approximations vary by up to $\sim 100\ \text{cm}^{-1}$ depending on the specific DFT functional

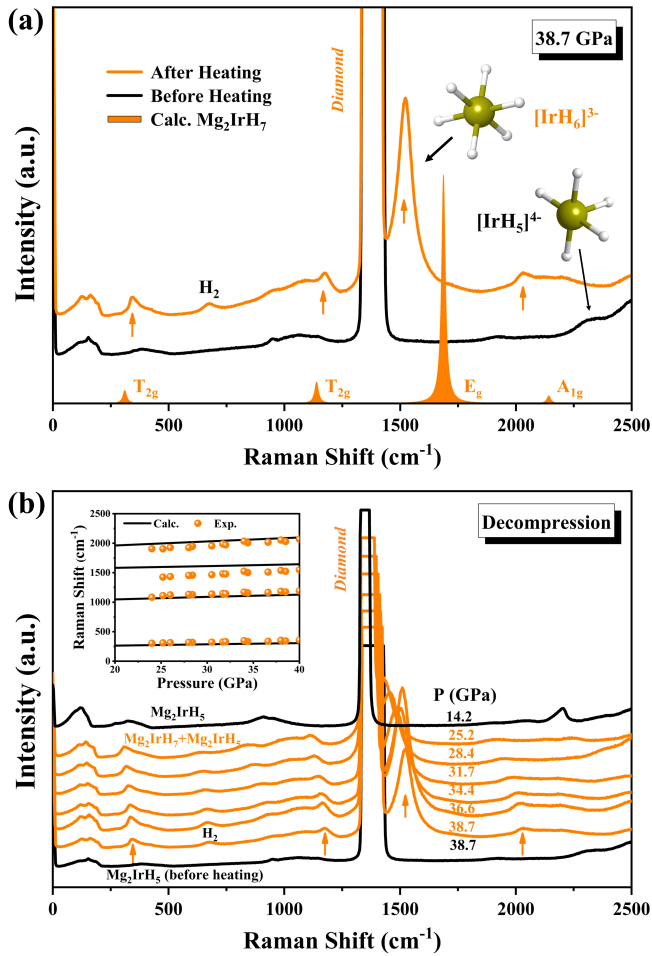


FIG. 2. (a) Experimental Raman spectra of Mg_2IrH_5 before and after heating at 38.7 GPa in ammonia borane. The calculated spectrum of Mg_2IrH_7 is shown for comparison using Lorentzian peak shapes with arbitrary widths. Orange arrows highlight new peaks attributed to $[\text{IrH}_6]_{3-}$ observed after heating. (b) Raman spectra of a heated sample obtained at room temperature while decompressing from 38.7 GPa. The inset compares experimental peak positions for Mg_2IrH_7 (points) with DFT-calculated (QE-PBE) frequencies (lines).

(e.g., PBE vs. BLYP) and code (e.g., CASTEP vs. QUANTUM ESPRESSO).

Observed across multiple independent experiments, the Raman frequencies of the four new peaks systematically decrease upon decompression and, below ~ 20 GPa, the system reproducibly reverts to Mg_2IrH_5 (Fig. 2(b) and Fig. S1). This reverse transformation is evidenced by the reappearance of the diagnostic $[\text{IrH}_5]_{4-}$ stretching band near 2200 cm^{-1} . The reversion to Mg_2IrH_5 during decompression at room temperature is indicative of a low energy barrier and supportive of the Mg_2IrH_7 Raman interpretation given the strong structural similarity between the two phases. The pressure dependence of the four observed Raman peaks, which track calculated mode frequencies (Fig. 2(b), inset), further supports the

formation of Mg_2IrH_7 .

To elucidate the structure of the new compound formed near 40 GPa, we performed *in situ* synchrotron XRD measurements on samples loaded in hydrogen. Before heating at 38 GPa, samples are well characterized by FCC Mg_2IrH_5 with broadened Bragg peaks, see Fig. S2 in Supplementary Material. Some regions of the sample contained small amount of metallic Ir or MgIrH_x impurities, also present in the starting precursor. The lattice parameter (see more structural details in Table S1) of $a = 6.032(5)\text{ \AA}$ is in good agreement with extrapolations from the previous report [21].

Immediately upon heating samples at the lowest laser powers possible (i.e., $T < 1000\text{ K}$), we observed the dis-

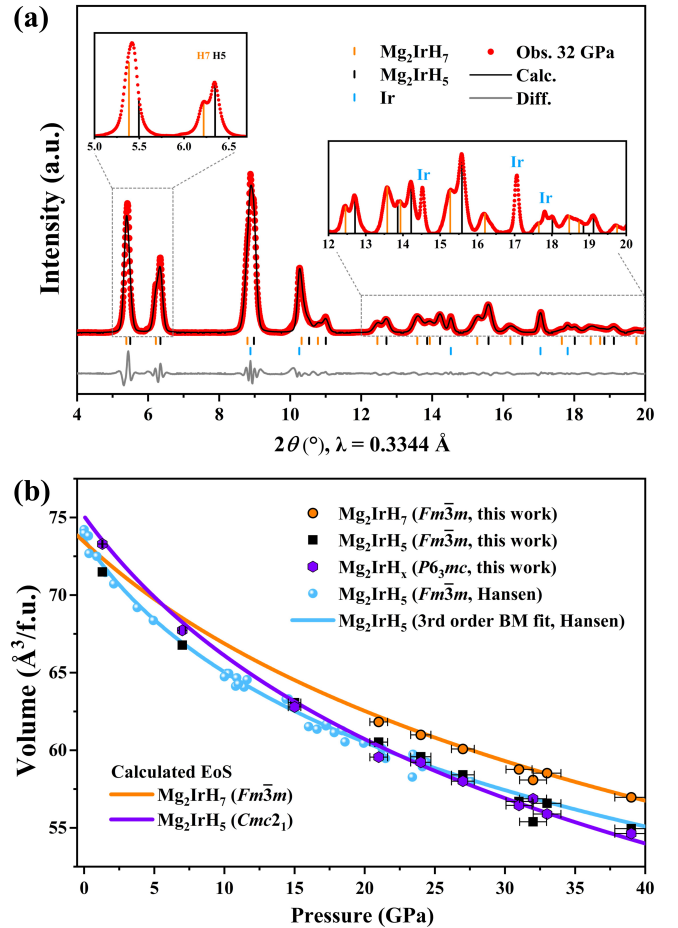


FIG. 3. (a) Representative XRD pattern showing the formation of an expanded FCC phase after heating Mg_2IrH_5 in hydrogen. The sample pressure dropped from 40 GPa to 32 GPa after heating. The red points correspond to the experimental data, while the black and gray curves represent the refinement and residual, respectively. Orange, black, and blue ticks indicate the calculated peak positions for Mg_2IrH_7 , Mg_2IrH_5 and Ir. (b) Volume per formula unit plotted as a function of pressure for Mg_2IrH_5 , [21] Mg_2IrH_7 , and hexagonal Mg_2IrH_x . The orange and purple lines show the DFT-calculated equations of state. Ordered $Cmc2_1$ Mg_2IrH_5 is used to approximate the disordered hexagonal variation.

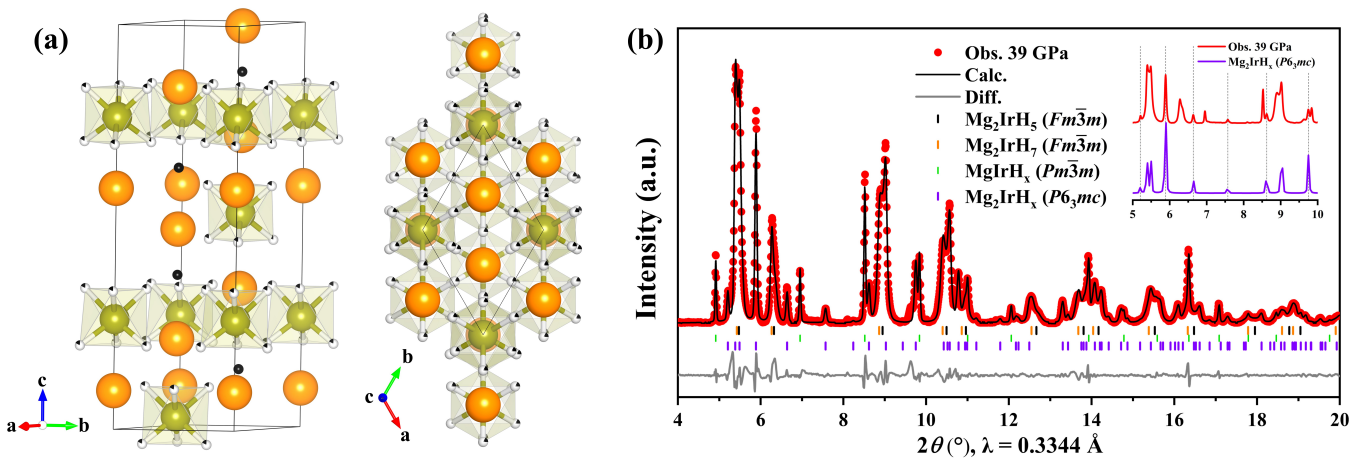


FIG. 4. (a) Crystal structure of $P6_3mc$ Mg_2IrH_x . The calculated $P6_3mc$ Mg_2IrH_7 structure possesses $[IrH_6]^{3-}$ units and interstitial H atoms (black spheres), like $Fm\bar{3}m$ Mg_2IrH_7 . In space group $P6_3mc$, Mg_2IrH_5 contains disordered $[IrH_5]^{4-}$ units (i.e., $\frac{5}{6}$ H occupancy represented by pie-chart spheres) with no interstitial hydrogen and can be described as an ordered orthorhombic $Cmc2_1$ structure in calculations. (b) Representative powder XRD pattern obtained after laser heating the samples to 1500 K and corresponding Le Bail refinement. The red points correspond to the experimental data, while the black and gray curves represent the refinement and residual, respectively. Orange, black, green, and purple ticks indicate the calculated peak positions for $Fm\bar{3}m$ Mg_2IrH_7 , $Fm\bar{3}m$ Mg_2IrH_5 , $Pm\bar{3}m$ $MgIrH_x$, and $P6_3mc$ Mg_2IrH_x . Inset: comparison of experimental data and calculated powder intensity profile for the $P6_3mc$ structure. Dashed lines mark select predicted Bragg positions for the $P6_3mc$ structure that do not overlap with coexisting phases.

tinct splitting of the FCC peaks (Fig. 3(a)), indicating the formation of a second, expanded FCC phase with $a = 6.179$ Å. The presence of these new FCC peaks are coincident with the formation of the new Raman peaks described above, particularly the diagnostic peak near 1500 cm^{-1} attributed to $[IrH_6]^{3-}$ stretching. The observed volume expansion from Mg_2IrH_5 to Mg_2IrH_7 is consistent with DFT calculations, which indicate a 3.9% volume increase at 40 GPa.

The expanded FCC lattice persists during decompression, tracking the DFT-calculated equation of state for Mg_2IrH_7 (Fig. 3(b)), until approximately 20 GPa. Below this pressure, the expanded lattice vanishes and only Mg_2IrH_5 was observed. The correspondence between XRD and Raman measurements allow us to confidently attribute the observed Raman modes to the expanded FCC phase, and agreement with DFT calculations strongly supports the assignment of this phase to FCC Mg_2IrH_7 .

Additional heating of samples (i.e., $T > 1000$ K) resulted in the formation of a more complex phase with many diffraction peaks (Fig. 4(b) and Fig. S3). The appearance of this phase was observed in some locations using the lowest heating powers and its formation is difficult to avoid, though it is favored at higher temperatures. Using single-crystal diffraction techniques with multigrain analysis on a sample heated near 1500 K, we were able to index this phase to a hexagonal lattice with $a = 4.31$ Å and $c = 14.2$ Å at 32 GPa, reproduced for a total of 22 grains at three sample positions. A tentative structural solution was obtained via intrinsic phasing, however subsequent refinements failed to converge with high reliabil-

ity (see Table S2). Nevertheless, the analysis provides useful insights into the metal substructure, which apparently maintains the starting Mg_2Ir composition ($Z = 4$) in the likely space group $P6_3mc$ with three Mg atoms located on the $2b$ positions ($z \approx 0.22, 0.36, \text{ and } 0.38$), one Mg atom on the $2a$ position ($z \approx 0.095$), and two Ir atoms on the $2a$ and $2b$ positions ($z \approx 0.29$ and 0.54 , respectively). The metal substructure contains several voids large enough to host hydrogen atoms.

While we were unable to explicitly solve the crystal structure and hydrogen content of this hexagonal phase, we performed constrained AIRSS runs, informed by the hexagonal experimental lattice, finding low-energy candidate structures that match the experimental observations. Interestingly, two of the compounds have the compositions Mg_2IrH_6 and Mg_2IrH_7 with space group $P6_3mc$ and atomic metal positions similar to those produced by experiments (see Supplemental Information). At 30 GPa, these phases are located 30–40 meV/atom above the convex hull and may be viewed as hexagonal transformations of the FCC phases with a doubling of the c -axis. While this hexagonal variation was not predicted for Mg_2IrH_5 , an orthorhombic $Cmc2_1$ phase with this composition was found with similar lattice vectors (see Table S3) following $b_{ortho} \approx b_{hex}\sqrt{3}$. Similar to the case of FCC Mg_2IrH_5 —where an ordered tetragonal structure was calculated to approximate the disordered FCC compound observed experimentally—this ordered $Cmc2_1$ version of Mg_2IrH_5 may represent a disordered hexagonal structure that is favored at finite temperature. Based on observed formula unit volumes of the hexagonal phase with pressure, the Mg_2IrH_5 composition is in good agreement with cal-

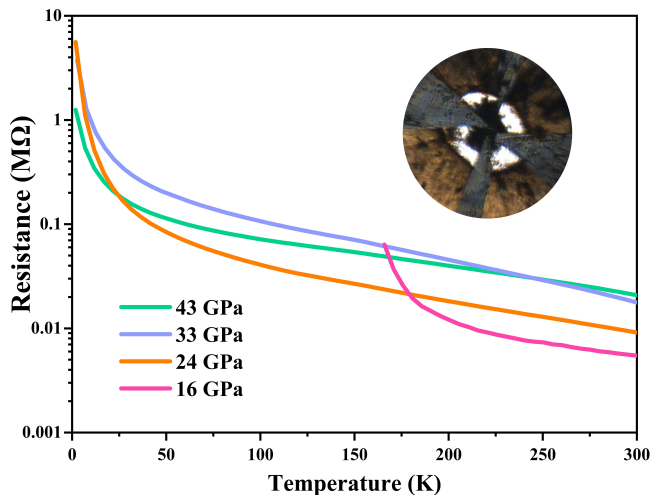


FIG. 5. Temperature-dependent electrical transport measurements performed after the synthesis of FCC Mg_2IrH_7 at 43 GPa and at subsequent decompression steps. Inset: Mg_2IrH_5 sample pellet with electrical contacts embedded in ammonia borane. The culet diameter is 300 μm .

culations (Fig. 3(b)). In this case, the hexagonal phase can represent a hexagonal arrangement of the disordered FCC Mg_2IrH_5 structure that becomes more favorable around 40 GPa, similar to pressure-induced martensitic transformations observed for noble gases [46, 47].

The observation of this hexagonal structure raises the question of whether the observed Raman modes described above could be attributed to this phase. In addition to the observation of the disappearance of these Raman modes at 20 GPa, coincident with the disappearance of the expanded FCC lattice by XRD at the same pressure, this possibility is ruled out by the preservation of the hexagonal phase to lower pressures by XRD. Hexagonal Mg_2IrH_x was observed to the lowest measured pressure (1.3 GPa), well beyond the disappearance of the Raman spectrum attributed to cubic Mg_2IrH_7 . If the composition of the hexagonal phase is indeed Mg_2IrH_5 , as supported by obtained diffraction volumes, it is likely that molecular Raman modes would largely coincide with FCC Mg_2IrH_5 given the presence of identical, disordered constituents.

Finally, the formation of FCC Mg_2IrH_7 allows us to begin the exploration of synthetic pathways to superconducting Mg_2IrH_6 via hydrogen removal, as initially proposed by Dolui et al. [13]. Given the structural similarity with Mg_2IrH_6 , diffusion of the non-covalent hydrogen from Mg_2IrH_7 represents a potential route to obtain this superconducting metastable phase. This possibility might be realized via the decompression of Mg_2IrH_7 given the local, low-energy minimum of Mg_2IrH_6 before reversion to Mg_2IrH_5 , and would be manifested by a change to metallic conductivity/superconductivity at some intermediate pressure.

To study this possibility, the behavior of Mg_2IrH_7 was investigated using electrical transport measurements. A

Mg_2IrH_5 sample equipped with electrical contacts was heated in ammonia borane near 40 GPa and the presence of an expanded FCC lattice was verified by XRD, in addition to the presence of the strong $\sim 1520\text{ cm}^{-1}$ Raman mode mapped across the sample. Temperature-dependent transport measurements near 40 GPa show insulating behavior with resistance reaching the $\text{M}\Omega$ level at low temperature (Fig. 5)—the expected behavior for FCC Mg_2IrH_7 , which is predicted to be a charge-balanced insulator (i.e., $2\text{Mg}^{2+}\cdot[\text{IrH}_6]^{3-}\cdot\text{H}^-$) with a PBE-DFT-predicted band gap of 2.46 eV.

When temperature-dependent transport measurements were conducted on Mg_2IrH_7 at pressure steps during decompression, the sample remained insulating with an offset in the resistance magnitude across the ~ 20 GPa decomposition threshold, presumably related to hydrogen loss and the reversion back to the Mg_2IrH_5 structure. Thus, the formation of Mg_2IrH_6 does not appear to occur spontaneously at room temperature based on decompression measurements performed across the pressure stability field. Future measurements focused on the kinetics and detailed $\text{Mg}_2\text{IrH}_7 \rightarrow \text{Mg}_2\text{IrH}_5$ transition mechanism could produce valuable insights for the transient stabilization of superconducting Mg_2IrH_6 .

While metastable Mg_2IrH_6 remains elusive to date, the demonstration of two nearly identical structures is promising for its future synthesis. FCC Mg_2IrH_5 , and now, Mg_2IrH_7 are available as starting precursors with isostructural metal substructure arrangements, differing only by a single hydrogen atom per formula unit. Non-equilibrium processing methods such as implantation/irradiation, deposition, electro/mechanochemistry, or dynamic P/T cycling might serve as valuable routes to be explored to isolate this exceptional, dynamically stable phase.

IV. CONCLUSION

Following prior studies on FCC Mg_2IrH_5 , $Fm\bar{3}m$ Mg_2IrH_7 was found to form at higher pressures near 40 GPa. The Raman spectrum of Mg_2IrH_7 is characterized by an intense Ir–H stretching band near 1520 cm^{-1} , diagnostic of $[\text{IrH}_6]^{3-}$ complexes, clearly distinguishing this phase from Mg_2IrH_5 . Compared with FCC Mg_2IrH_5 , Mg_2IrH_7 has an expanded lattice and persists to ca. 20 GPa when decompressed at room temperature. In addition to FCC Mg_2IrH_7 , another hexagonal Mg_2IrH_x hydride was observed upon heating samples near 40 GPa. This structure crystallizes in the probable space group $P6_3mc$ with the likely composition Mg_2IrH_5 based on formula-unit volume, and likely represents a hexagonal modification of disordered FCC Mg_2IrH_5 with a doubling of the c -axis. The thermodynamic stability, spectroscopic behavior and structural observations in this work are all strongly supported by *ab initio* calculations, providing further confidence in experimental interpretations and in using these tools to help guide materials discovery. While

superconducting Mg_2IrH_6 was not observed as a spontaneous intermediate phase during the decompression of Mg_2IrH_7 , the successful formation of Mg_2IrH_7 enables access to a structurally related compound that may serve as a useful precursor for future non-equilibrium synthesis approaches.

ACKNOWLEDGMENTS

This work was supported by the Deep Science Fund of Intellectual Ventures. We acknowledge the GeoSoilEnviroCARS (The University of Chicago, Sector 13), Advanced Photon Source, Argonne National Laboratory for provision of synchrotron radiation facilities at beamline.

GeoSoilEnviroCARS is supported by the National Science Foundation – Earth Sciences via SEES: Synchrotron Earth and Environmental Science (EAR–2223273). This research used resources of the Advanced Photon Source, a U.S. Department of Energy (DOE) Office of Science User Facility operated for the DOE Office of Science by Argonne National Laboratory under Contract No. DE-AC02-06CH11357. Use of the GSECARS Raman Lab System was supported by the NSF MRI Proposal (EAR-1531583). This research also used resources of the Advanced Light Source, a U.S. DOE Office of Science User Facility under contract no. DE-AC02-05CH11231. The authors thank Bora Kalkan and Martin Kunz for assistance with XRD measurements and Amol Karandikar for assistance with CO_2 laser heating.

-
- [1] A. Drozdov, M. Erements, I. Troyan, V. Ksenofontov, and S. I. Shylin, Conventional superconductivity at 203 kelvin at high pressures in the sulfur hydride system, *Nature* **525**, 73 (2015).
- [2] M. Somayazulu, M. Ahart, A. K. Mishra, Z. M. Geballe, M. Baldini, Y. Meng, V. V. Struzhkin, and R. J. Hemley, Evidence for superconductivity above 260 K in lanthanum superhydride at megabar pressures, *Phys. Rev. Lett.* **122**, 027001 (2019).
- [3] P. Kong, V. S. Minkov, M. A. Kuzovnikov, A. P. Drozdov, S. P. Besedin, S. Mozaffari, L. Balicas, F. F. Balakirev, V. B. Prakapenka, S. Chariton, *et al.*, Superconductivity up to 243 K in the yttrium-hydrogen system under high pressure, *Nat. Commun.* **12**, 5075 (2021).
- [4] F. Peng, Y. Sun, C. J. Pickard, R. J. Needs, Q. Wu, and Y. Ma, Hydrogen clathrate structures in rare earth hydrides at high pressures: Possible route to room-temperature superconductivity, *Phys. Rev. Lett.* **119**, 107001 (2017).
- [5] L. Ma, K. Wang, Y. Xie, X. Yang, Y. Wang, M. Zhou, H. Liu, X. Yu, Y. Zhao, H. Wang, *et al.*, High-temperature superconducting phase in clathrate calcium hydride CaH_6 up to 215 K at a pressure of 172 GPa, *Phys. Rev. Lett.* **128**, 167001 (2022).
- [6] D. V. Semenok, I. A. Troyan, D. Zhou, A. V. Sadakov, K. S. Pervakov, O. A. Sobolevskiy, A. G. Ivanova, M. Galasso, F. G. Alabarse, W. Chen, *et al.*, Ternary superhydrides under pressure of anderson’s theorem: Near-record superconductivity in $(\text{La,Sc})\text{H}_{12}$, *Adv. Funct. Mater.* **35**, 2504748 (2025).
- [7] Y. Song, C. Ma, H. Wang, M. Zhou, Y. Qi, W. Cao, S. Li, H. Liu, G. Liu, and Y. Ma, Room-temperature superconductivity at 298K in ternary La-Sc-H system at high-pressure conditions (2025), arXiv:2510.01273 [cond-mat.supr-con].
- [8] C. W. Chu, L. Z. Deng, and Z. Wu, The retention and study of high-pressure-induced phases in high- and room-temperature superconductors, *J. Supercond. Nov. Magn.* **35**, 987 (2022).
- [9] Y. Deng and M. B. Maple, Bringing pressure-induced superconductivity back to ambient pressure, *Proc. Natl. Acad. Sci. U.S.A.* **122**, e2501048122 (2025).
- [10] Y. Song, J. Bi, Y. Nakamoto, K. Shimizu, H. Liu, B. Zou, G. Liu, H. Wang, and Y. Ma, Stoichiometric ternary superhydride LaBeH_8 as a new template for high-temperature superconductivity at 110 K under 80 GPa, *Phys. Rev. Lett.* **130**, 266001 (2023).
- [11] X. Song, X. Hao, X. Wei, X.-L. He, H. Liu, L. Ma, G. Liu, H. Wang, J. Niu, S. Wang, *et al.*, Superconductivity above 105 K in nonclathrate ternary lanthanum borohydride below megabar pressure, *J. Am. Chem. Soc.* **146**, 13797 (2024).
- [12] A. Sanna, T. F. Cerqueira, Y.-W. Fang, I. Errea, A. Ludwig, and M. A. Marques, Prediction of ambient pressure conventional superconductivity above 80 K in hydride compounds, *npj Comput. Mater.* **10**, 44 (2024).
- [13] K. Dolui, L. J. Conway, C. Heil, T. A. Strobel, R. P. Prasankumar, and C. J. Pickard, Feasible route to high-temperature ambient-pressure hydride superconductivity, *Phys. Rev. Lett.* **132**, 166001 (2024).
- [14] F. Zheng, Z. Zhang, Z. Wu, S. Wu, Q. Lin, R. Wang, Y. Fang, C.-Z. Wang, V. Antropov, Y. Sun, *et al.*, Prediction of ambient pressure superconductivity in cubic ternary hydrides with MH_6 octahedra, *Mater. Today Phys.* **42**, 101374 (2024).
- [15] B. Li, Y. Fan, J. Zhai, Z. Cao, C. Zhu, J. Cheng, S. Liu, and Z. Shi, Prediction of High-Temperature Superconductivity in Cubic Ternary Hydride M_3XH_8 at Ambient Pressure, *J. Phys. Chem. C* **129**, 7098 (2025).
- [16] B. Li, C. Zhu, J. Zhai, C. Yin, Y. Fan, J. Cheng, S. Liu, and Z. Shi, Theoretical prediction of high-temperature superconductivity in SrAuH_3 at ambient pressure, *Phys. Rev. B* **110**, 214504 (2024).
- [17] Đorđe Dangić, Y.-W. Fang, T. F. Cerqueira, A. Sanna, T. Novoa, H. Gao, M. A. Marques, and I. Errea, Ambient pressure high temperature superconductivity in RbPH_3 facilitated by ionic anharmonicity, *Comput. Mater. Today*, 100043 (2025).
- [18] T. Muramatsu, W. K. Wanene, M. Somayazulu, E. Vinitzky, D. Chandra, T. A. Strobel, V. V. Struzhkin, and R. J. Hemley, Metallization and superconductivity in the hydrogen-rich ionic salt BaReH_9 , *J. Phys. Chem. C* **119**, 18007 (2015).
- [19] D. Meng, M. Sakata, K. Shimizu, Y. Iijima, H. Saitoh, T. Sato, S. Takagi, and S.-i. Orimo, Superconductivity

- of the hydrogen-rich metal hydride $\text{Li}_5\text{MoH}_{11}$ under high pressure, *Physical Review B* **99**, 024508 (2019).
- [20] W. Lu, M. J. Hutcheon, M. F. Hansen, K. Dolui, S. Sinha, M. R. Sahoo, C. J. Pickard, C. Heil, A. Pakhomova, M. Mezouar, D. Daisenberger, S. Chariton, V. Prakapenka, M. N. Julian, R. P. Prasankumar, and T. A. Strobel, Prediction and synthesis of $\text{Mg}_4\text{Pt}_3\text{H}_6$: A superconducting complex transition metal hydride stabilized at ambient pressure, *Phys. Rev. B* **112**, 094513 (2025).
- [21] M. F. Hansen, L. J. Conway, K. Dolui, C. Heil, C. J. Pickard, A. Pakhomova, M. Mezouar, M. Kunz, R. P. Prasankumar, and T. A. Strobel, Synthesis of Mg_2IrH_5 : A potential pathway to high- T_c hydride superconductivity at ambient pressure, *Phys. Rev. B* **110**, 214513 (2024).
- [22] X. Wang, W. E. Pickett, M. Hutcheon, R. P. Prasankumar, and E. Zurek, Why mg_2IrH_6 is predicted to be a high-temperature superconductor, but ca_2IrH_6 is not, *Angewandte Chemie International Edition* **63**, e202412687 (2024), <https://onlinelibrary.wiley.com/doi/pdf/10.1002/anie.202412687>.
- [23] H. K. Mao, J. Xu, and P. M. Bell, Calibration of the ruby pressure gauge to 800 kbar under quasi-hydrostatic conditions, *J. Geophys. Res.* **91**, 4673 (1986).
- [24] Y. Akahama and H. Kawamura, Pressure calibration of diamond anvil raman gauge to 410 GPa, *J. Phys.: Conf. Ser.* **215**, 012195 (2010).
- [25] V. B. Prakapenka, A. Kubo, A. Kuznetsov, A. Laskin, O. Shkurikhin, P. Dera, M. L. Rivers, and S. R. Sutton, Advanced flat top laser heating system for high pressure research at GSECARS: application to the melting behavior of germanium, *High Pressure Research* **28**, 225 (2008).
- [26] C. Prescher and V. B. Prakapenka, DIOPTAS: a program for reduction of two-dimensional X-ray diffraction data and data exploration, *High Pressure Research* **35**, 223 (2015).
- [27] M. Kunz, A. A. MacDowell, W. A. Caldwell, D. Cambie, R. S. Celestre, E. E. Domning, R. M. Duarte, A. E. Gleason, J. M. Glossinger, N. Kelez, D. W. Plate, T. Yu, J. M. Zaug, H. A. Padmore, R. Jeanloz, A. P. Alivisatos, and S. M. Clark, A beamline for high-pressure studies at the Advanced Light Source with a superconducting bending magnet as the source, *J. of Synchrotron Radiat.* **12**, 650 (2005).
- [28] V. Monteseuro, J. A. Sans, V. Cuartero, F. Cova, I. A. Abrikosov, W. Olovsson, C. Popescu, S. Pascarelli, G. Garbarino, H. J. M. Jönsson, T. Irifune, and D. Errandonea, Phase stability and electronic structure of iridium metal at the megabar range, *Sci. Rep.* **9**, 8940 (2019).
- [29] B. H. Toby and R. B. Von Dreele, GSAS-II: the genesis of a modern open-source all purpose crystallography software package, *J Appl Crystallogr.* **46**, 544 (2013).
- [30] A. Aslandukov, M. Aslandukov, N. Dubrovinskaia, and L. Dubrovinsky, *Domain Auto Finder (DAFi)* program: the analysis of single-crystal X-ray diffraction data from polycrystalline samples, *J Appl Crystallogr.* **55**, 1383 (2022).
- [31] CrysAlisPro Software system ver. 1.171.42, rigaku oxford diffraction (2023).
- [32] G. M. Sheldrick, Crystal structure refinement with *SHELXL*, *Acta Crystallogr. C* **71**, 3 (2015).
- [33] G. M. Sheldrick, *SHELXT* – Integrated space-group and crystal-structure determination, *Acta Crystallogr. A* **71**, 3 (2015).
- [34] O. V. Dolomanov, L. J. Bourhis, R. J. Gildea, J. A. K. Howard, and H. Puschmann, *OLEX2*: a complete structure solution, refinement and analysis program, *J Appl Crystallogr.* **42**, 339 (2009).
- [35] L. J. van der PAUW, A method of measuring specific resistivity and Hall effect of discs of arbitrary shape, in *Semiconductor Devices: Pioneering Papers*, pp. 174–182.
- [36] S. J. Clark, M. D. Segall, C. J. Pickard, P. J. Hasnip, M. I. Probert, K. Refson, and M. C. Payne, First principles methods using CASTEP, *Z. Kristallogr. Cryst. Mater.* **220**, 567 (2005).
- [37] J. P. Perdew, A. Ruzsinszky, G. I. Csonka, O. A. Vydrov, G. E. Scuseria, L. A. Constantin, X. Zhou, and K. Burke, Restoring the density-gradient expansion for exchange in solids and surfaces, *Phys. Rev. Lett.* **100**, 136406 (2008).
- [38] K. Refson, P. R. Tulip, and S. J. Clark, Variational density-functional perturbation theory for dielectrics and lattice dynamics, *Phys. Rev. B* **73**, 155114 (2006).
- [39] P. Giannozzi, S. Baroni, N. Bonini, M. Calandra, R. Car, C. Cavazzoni, D. Ceresoli, G. L. Chiarotti, M. Cococcioni, I. Dabo, *et al.*, QUANTUM ESPRESSO: a modular and open-source software project for quantum simulations of materials, *J. Phys.: Condens. Matter* **21**, 395502 (2009).
- [40] J. P. Perdew, K. Burke, and M. Ernzerhof, Generalized gradient approximation made simple, *Physical review letters* **77**, 3865 (1996).
- [41] K. F. Garrity, J. W. Bennett, K. M. Rabe, and D. Vanderbilt, Pseudopotentials for high-throughput dft calculations, *Computational Materials Science* **81**, 446 (2014).
- [42] S. F. Parker, K. P. J. Williams, M. Bortz, and K. Yvon, Inelastic Neutron Scattering, Infrared, and Raman Spectroscopic Studies of Mg_2FeH_6 and Mg_2FeD_6 , *Inorg. Chem.* **36**, 5218 (1997).
- [43] S. F. Parker, S. M. Bennington, A. J. Ramirez-Cuesta, G. Auffermann, W. Bronger, H. Herman, K. P. Williams, and T. Smith, Inelastic neutron scattering and Raman spectroscopies and periodic DFT studies of Rb_2PtH_6 and Rb_2PtD_6 , *J. Am. Chem. Soc.* **125**, 11656 (2003).
- [44] H. Hagemann and R. O. Moyer, Raman spectroscopy studies on M_2RuH_6 where $\text{M} = \text{Ca}, \text{Sr}, \text{and Eu}$, *Journal of alloys and compounds* **330**, 296 (2002).
- [45] S. F. Parker, Spectroscopy and bonding in ternary metal hydride complexes—Potential hydrogen storage media, *Coordination Chemistry Reviews* **254**, 215 (2010).
- [46] E. Kim, M. Nicol, H. Cynn, and C.-S. Yoo, Martensitic fcc-to-hcp transformations in solid xenon under pressure: A first-principles study, *Phys. Rev. Lett.* **96**, 035504 (2006).
- [47] A. D. Rosa, G. Garbarino, R. Briggs, V. Svitlyk, G. Morard, M. A. Bouhifd, J. Jacobs, T. Irifune, O. Mathon, and S. Pascarelli, Effect of the fcc-hcp martensitic transition on the equation of state of solid krypton up to 140 GPa, *Phys. Rev. B* **97**, 094115 (2018).